PNAS RESEARCH ARTICLE | BIOCHEMISTRY OPEN ACCESS

Apurinic/Apyrimidinic Endodeoxyribonuclease 1 modulates RNA G-quadruplex folding of miR-92b and controls its expression in cancer cells

Alessia Bellina[a,1], Matilde Clarissa Malfatti[a,b,1], Gilmar Salgado[c], Aaron M. Fleming[d], Giulia Antoniali[a], Zahraa Othman[c], Nicolò Gualandi[a], Sara La Manna[e], Daniela Marasco[e], Erik Dassi[f], Cynthia J. Burrows[d,2], and Gianluca Tell[a,2]

Affiliations are included on p. 11.

Edited by Lydia Contreras, The University of Texas at Austin, Austin, TX; received December 14, 2023; accepted October 9, 2024 by Editorial Board Member Marlene Belfort

In the last decade, several novel functions of the mammalian Apurinic/Apyrimidinic Endodeoxyribonuclease 1 (APE1) have been discovered, going far beyond its canonical function as DNA repair enzyme and unveiling its potential roles in cancer development. Indeed, it was shown to be involved in DNA G-quadruplex biology and RNA metabolism, most importantly in the miRNA maturation pathway and the decay of oxidized or abasic miRNAs during oxidative stress conditions. In recent years, several noncanonical pathways of miRNA biogenesis have emerged, with a specific focus on guanosine-rich precursors that can form RNA G-quadruplex (rG4) structures. Here, we show that several miRNA precursors, dysregulated upon APE1 depletion, contain an rG4 motif and that their corresponding target genes are up-regulated after APE1 depletion. We also demonstrate, both by in vitro assays and by using different cancer cell lines, that APE1 can modulate the folding of an rG4 structure contained in pre-miR-92b, with a mechanism strictly dependent on lysine residues present in its N-terminal disordered region. Furthermore, APE1 cellular depletion alters the maturation process of miR-92b, mainly affecting the shuttling between the nucleus and cytosol. Bioinformatic analysis of APE1-regulated rG4-containing miRNAs supports the relevance of our findings in cancer biology. Specifically, these miRNAs exhibit high prognostic significance in lung, cervical, and liver tumors, as suggested by their involvement in several cancer-related pathways.

APE1 | rG4 | miRNA | gene expression | oxidative stress

Significance

We highlight a noncanonical role of APE1 on miRNA precursors containing RNA G-quadruplex (rG4) structures. Specifically, APE1 modulates their folding, mainly through its N-terminal region and some residues in its catalytic domain. Moreover, we demonstrate that APE1 regulates the shuttling and accumulation of miR-92b between the nuclear and cytosolic compartments, opening unique perspectives on how APE1 may exercise its role in the miRNA maturation pathway. Additionally, miRNAs with rG4 motifs in their precursors dysregulated after APE1 depletion have significant prognostic value in real-world tumors, suggesting potential targets for cancer therapy. Since massive oxidation occurs during oxidative stress conditions, this work lays the basis for understanding the rG4-mediated mechanism of miRNA regulation.

In humans, a large quota of RNAs is not translated into proteins and constitutes the noncoding fraction of RNAs (1). Within this class, microRNAs (miRNAs) and their precursors emerge for their increasingly recognized roles, being involved in several physiological and pathological processes (2, 3). miRNA biogenesis is finely regulated, starting with the RNA polymerase II–mediated transcription of a primary miRNA (pri-miRNA) that folds into a stem-loop structure, recognized and cropped by the Drosha-DGCR8 complex (4). The resulting transcript, called precursor miRNA (pre-miRNA), is exported to the cytoplasm, where its terminal loop is cleaved by Dicer, releasing a small duplex RNA, which is then loaded onto the Argonaute protein and, after the removal of one of the two strands, becomes part of the mature RNA-induced silencing complex (RISC) to specifically target the mRNA molecules based on complementarity with the seed region (5).

Recent studies have described an alternative pathway of miRNA maturation specifically tuned to guanosine-rich pre-miRNAs, which involves the existence of a thermodynamic equilibrium between the canonical stem-loop and a noncanonical secondary structure called RNA G-quadruplex (rG4) (6). Analogously to DNA G-quadruplexes (G4s), rG4s are composed of stacks of guanine tetrads (called G-quartets) linked by Hoogsteen hydrogen bonds, mostly folded in a parallel topology with all strands following the same direction (7). Interestingly, this folded structure is more stable and compact than its DNA analogue, principally due to the 2' hydroxyl group of the ribose (8). Several studies have shown that the presence of rG4s in miRNAs may affect their maturation process (6). Indeed, if present in pri-miRNAs, rG4s can inhibit Drosha-DGCR8 processing (9, 10); once present in pre-miRNAs, rG4s can inhibit Dicer activity (8, 11); whereas in mature miRNAs, rG4s can impede loading onto the RISC (12). Therefore, the consequence of this multilevel inhibition may lead to an aberrant miRNA maturation, impairing their ability to target mRNAs, thus potentially affecting several cellular pathways (13, 14). For these reasons, targeting rG4s in miRNAs and their precursors could be explored as a eligible therapeutic strategy. A very well-characterized example is represented by

The authors declare no competing interest.

This article is a PNAS Direct Submission L.M.C. is a guest editor invited by the Editorial Board.

[1]A.B. and M.C.M. contributed equally to this work.

[2]To whom correspondence may be addressed. Email: burrows@chem.utah.edu or gianluca.tell@uniud.it.

This article contains supporting information online at https://www.pnas.org/lookup/suppl/doi:10.1073/pnas.2317861121/-/DCSupplemental.

Published November 4, 2024.

pre-miR-92b, which is structured to form a stable rG4 at physiological KCl concentrations (15). Mature miR-92b is clinically relevant, being overexpressed in several human cancers including cervical and gastric cancers, glioma, and non–small cell lung cancer (NSCLC) (16–18). It was shown that the stabilization of its rG4 by a locked nucleic acid resulted in a decreased maturation of the miR-92b itself, leading to the rescue of the expression of its target PTEN, thus sensitizing NSCLC cells to doxorubicin treatment (19).

APE1/Ref1 (Apurinic/Apyrimidinic Endodeoxyribonuclease/Redox Effector Factor 1) is a multifunctional protein, mostly known for its role as endonuclease in the base excision repair (BER) pathway, deputed to the repair of oxidative and nondistorting DNA lesions, and functioning as a redox hub for many transcription factors (TFs) (20). In recent years, great attention has been paid to the noncanonical roles of APE1 (20, 21). Indeed, APE1 mediates transcriptional regulation by modulating G4s at promoter regions and creating a platform for TF recruitment (22–24). In vitro experiments have demonstrated that APE1 maintains its endonuclease activity toward abasic (e.g., AP) sites embedded in G4s, although with a lower efficiency when compared to duplex DNA (25, 26). Surprisingly, the N-terminal region of APE1 is essential not only for G4s binding but also for modulating the catalysis of the AP site cleavage. Remarkably, those activities largely depend on the ionic strength of the reaction and, above all, on the magnesium concentration (23, 25). Furthermore, the N-terminal portion of the protein presents several lysine residues, whose acetylation increased the cleavage ability of the protein and diminished the capacity to bind chromatin, due to the neutralization of its positive charges (25). Most interestingly, APE1 is involved in oxidized or abasic-pri-miRNA processing and stability during oxidative stress (27). Data from our laboratory have demonstrated that APE1 efficiently binds to pri-miR-221 and pri-miR-222 in HeLa, HCT-116, and MCF-7 cell lines and that their processing is affected in APE1-depleted cells, resulting in an upregulation of PTEN, a target gene of both miRNAs, during oxidative stress conditions. Moreover, we showed that APE1 interacts with Drosha but not with DGCR8 and DDX5, suggesting that may affect the early phases of the microprocessor pathway and may compete with Dicer for the processing of some pre-miRNAs (27). Finally, APE1 is involved in controlling Dicer expression in NSCLC through APE1-regulated miRNA-33a-5p and miRNA-130b, thus contributing to epithelial–mesenchymal transition (EMT) mechanisms in cancer cells (28). Several studies have established that APE1, which is overexpressed in the nucleus and cytoplasm of many tumor types (e.g., hepatic, cervical, and lung), is involved in tumor progression (29–32), thus representing an important target for cancer therapy (21). However, the molecular mechanisms responsible for the tumorigenic role of APE1 are still unclear but point to the not-repair-related activities of the protein, including redox regulation and RNA metabolism. Recent data, including ours, suggest that APE1 may contribute to the expression of chemoresistance and tumor progression genes through posttranscriptional mechanisms involving miRNA regulation (27, 33, 34). To date, it is unknown whether APE1 is endowed with the ability to recognize oncogenic miRNAs (onco-miRNAs) in a sequence-specific manner or whether the presence of rG4s may play a role in its binding properties. Shedding light on these aspects could contribute to understanding the role of APE1 in the tumorigenic process. Moreover, it is known that oxidative stress can cause damage to both DNA and RNA with detrimental effects on gene expression that could lead to chemoresistance onset (35, 36). Accordingly, during oxidative stress exposure in cancer cells, damaged miRNAs might have important effects on gene expression (35, 37, 38). As recently proposed, miRNA-bearing lesions, including those containing AP sites or oxidized bases (e.g., 8-oxoG), seem to accumulate up to 10-fold or more during cancer development and oxidative stress exposure, acting as epitranscriptional regulators to rewire cancer gene expression (39). It is still unknown which proteins can specifically recognize and process oxidized miRNAs, whereas their in-depth study would be essential for understanding molecular mechanisms in miRNA quality control and developing eligible specific anticancer strategies. In addition, since AP sites or 8-oxoG could significantly impact the stability and forming potential of rG4 structures, it is imperative to inspect these issues from a functional perspective. In this context, the ability of APE1 to recognize and process damaged miRNAs (39), alone or in cooperation with other proteins, represents an interesting focus in cancer biology and a promising antitumoral target. Therefore, this study aims to investigate the involvement of APE1 in the stabilization/destabilization effect of pre-miRNAs containing rG4 motifs, as this protein might regulate the equilibrium between the G4 itself and the canonical stem-loop structure, thus impacting miRNA processing.

Through bioinformatic analysis performed on a list of differentially expressed miRNAs obtained from HeLa and A549 cells upon stable downregulation/reconstitution of APE1 protein (27, 28, 40), we investigated the presence of rG4s in pre-miRNAs, finding that about 27% of those precursors contain an rG4-forming motif. In vitro experiments, using a synthetic oligoribonucleotide mimicking the rG4-containing pre-miR-92b, showed that APE1 can modulate the folding and stability of this structure. In addition, we analyzed the region of APE1 that binds the rG4 motif contained in pre-miR-92b and compared this region with previously published contact surfaces between APE1 and different enzymatic targets such as DNA. Furthermore, we confirmed these data in HeLa cells by observing that APE1 can bind pri-miR-92b and that this binding is mainly mediated by lysine residues present in its unstructured N-terminal region. Finally, we showed that miR-92b subcellular localization in nuclei and cytosol is deeply influenced by APE1 expression, thus suggesting that APE1 could be an important regulator of miR-92b maturation and shuttling processes. A bioinformatic analysis, performed on the predicted rG4-containing miRNAs regulated by APE1, highlighted their prognostic significance in lung, cervical, and liver tumors. Finally, by functional enrichment analysis, we reported the involvement of these miRNAs in several cancer-related pathways, such as EMT, tumor progression, and immune evasion. All these results provide evidence for a unique layer of APE1 functions, which could mediate its role in cancer development.

Results

APE1 Depletion Causes a Dysregulation of rG4 Motif-Containing pre-miRNAs. Starting from a previously published list of miRNAs dysregulated upon APE1 depletion (n = 248, Dataset S1A) obtained by Nanostring and RNA-seq analysis in HeLa and A549 cell lines (27, 28, 40), we searched for their corresponding pre-miRNAs (n = 227) by using miRbase (41). Then, we examined the presence of rG4-forming motif sequences in the pre-miRNAs through a bioinformatic analysis using three algorithms (*Material and Methods*). In total, 61 of the initial 227 sequences were predicted to contain an rG4 motif at least by one tool, which indicated that about 27% of the pre-miRNAs, dysregulated by APE1 depletion, potentially contained an rG4 motif (Fig. 1*A* and Dataset S1B). Among 61 pre-miRNAs, 15 sequences were predicted by all three algorithms (6.6%) with above-threshold scores; 19 were predicted by both QGRS mapper and psqfinder (8.4%), while the remaining 27 were predicted by only one of the three tools (12%). We further observed that following APE1 depletion, the number of dysregulated pre-miRNAs holding

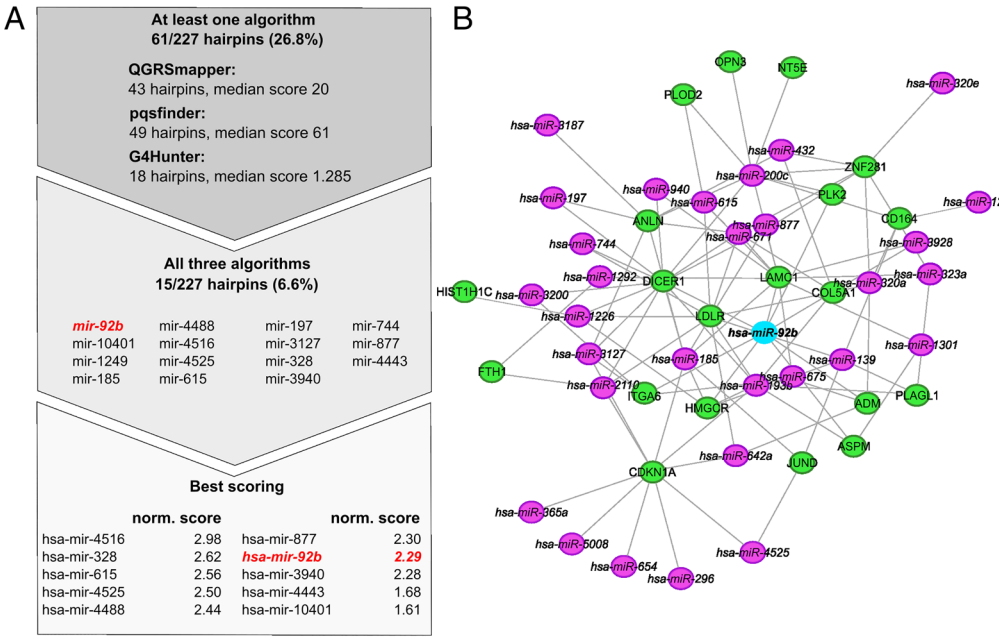

Fig. 1. Predicted rG4-containing pre-miRNAs dysregulated upon APE1 silencing control several up-regulated genes associated with APE1 depletion. (*A*) Number of rG4-containing pre-miRNAs predicted at least by one algorithm and the related median prediction score (*Top*); the list of pre-miRNAs predicted to have at least an rG4 by all three algorithms (*Center*); and the top ten pre-miRNA ranked by their normalized prediction score, computed as the sum of each algorithm's score scaled by the maximum obtained score for that algorithm (*Bottom*). (*B*) Network of miRNA–gene interaction for the 61 miRNA present in the signature. Only up-regulated genes (*P*-value < 0.05 and log2FoldChange > 0) in both of the cell lines analyzed (HeLa or A549) were reported. Each purple node represents a single miRNA while the edges represent the miRNA–gene target interaction reported in TarBase. Up-regulated genes are reported as green nodes.

rG4-forming sequences (26.8%) was comparable to the number of total predicted rG4-containing pre-miRNAs (27.5%) obtained from performing the same analysis on the whole human miRbase (Dataset S1 C and D), leading us to the hypothesis that APE1 has a molecular role in the regulation of a substantial number of rG4-containing miRNAs.

Next, to identify the pathways associated with up-regulated genes following APE1 depletion, we performed a pathway enrichment analysis, starting from experimentally tested target genes using the TarBase database (42), which houses a manually curated collection of experimentally tested miRNA targets. We then selected interactions that were already validated in human cells (*SI Appendix*, Fig. S1 and Dataset S2A). Genes exhibiting upregulation were defined as those having an adjusted *P*-value < 0.05 and a positive log2(Fold Change) in APE1-depleted cells, compared to control cells, in at least one of the two cell lines examined (HeLa or A549). Our findings revealed that the up-regulated genes primarily participate in oncogenic pathways such as the "p53 signaling pathway", "Pancreatic cancer", "Transcriptional misregulation in cancer", "Small cell lung cancer", "Proteoglycans in cancer", and "Colorectal cancer", further indicating the role of APE1 in cancer onset and progression (*SI Appendix*, Fig. S1). Notably, several up-regulated genes were significantly enriched in the "Focal adhesion" pathway, implicating a role of APE1 in processes related to extracellular matrix organization and cell-to-cell interactions, whose dysregulation could lead to different human diseases including cancer. Indeed, focal adhesion proteins contribute to multiple aspects of cancer, including increased cell proliferation, resistance to apoptosis, elevated cell motility and invasion, and promotion of angiogenesis (43). In line with this result, we also identified significantly enriched pathways related to senescence and the cell cycle, reinforcing the role of APE1 in those processes (*SI Appendix*, Fig. S1). Finally, to explore the relationship among up-regulated genes and dysregulated rG4-containing miRNAs upon APE1 depletion, we built a miRNA–gene interaction network (Fig. 1*B*) reporting the TarBase-validated interactions between each of the 61 rG4-containing miRNAs and the up-regulated genes in common between the HeLa and A549 cell lines after APE1 depletion (42). Notably, we observed the presence of different interactions between rG4-containing miRNAs and up-regulated genes following APE1 depletion. Intriguingly, miR-92b, located in the center of the network, regulates the expression of many up-regulated genes directly and indirectly, suggesting its pivotal role in the regulation of the expression of key genes associated with APE1 depletion (27) (Fig. 1*B*).

APE1 Binds pre-miR-92b and Modulates rG4 Conformational Changes. Given the role of APE1 in miRNA processing and in the regulation of G4 structures (23, 25–28), we investigated whether APE1 might bind rG4-containing miRNAs and modulate the folding of rG4 structures in miRNAs. To test this hypothesis, we chose pre-miR-92b as a general model for our next investigations for the following reasons: i) pre-miR-92b was predicted to contain an rG4 by all three tools with high scores and controls target genes already known to be regulated by APE1 (i.e., PTEN, DICER, CDKN1A); ii) pre-miR-92b contains an rG4 motif that was already experimentally validated and characterized (15); iii) the stabilization of its rG4 represents an attractive therapeutic target (15, 19); and iv) its mature form (miR-92b-3p) resulted dysregulated both in HeLa and A549 cell lines after APE1 depletion (27, 28, 40).

Based on the QGRSmapper analysis (reported in *SI Appendix*, Table S1), we first designed an rG4-forming sequence derived from pri-miR-92b and pre-miR-92b sequences (*SI Appendix*, Fig. S2*A*). This sequence, hereafter named pre-92b and highlighted in green, is entirely located in the pre-miR-92b sequence (*SI Appendix*, Table S1). This sequence was used for the following in vitro analyses with or without a fluorophore in the 5'-end. In our structure analysis, the nonfluorescent oligoribonucleotide was folded in a 50 mM K^+ solution and then inspected by Circular Dichroism (CD) and NMR spectroscopies. The CD spectrum showed a positive (λ_{max} = 263 nm) and a negative (λ_{min} = 242 nm) molar ellipticities, consistent with a parallel-stranded rG4 (*SI Appendix*, Fig. S2*B*) (44), as confirmed by 1D ^{1}H NMR spectrum, indicating the formation of several imino peaks compatible with two or more conformers of a three G-tetrad rG4 in dynamic equilibrium (*SI Appendix*, Fig. S2*C*).

Upon confirming the rG4-folding ability of the pre-miR-92b under these experimental conditions, we evaluated the ability of APE1 to bind the pre-miR-92b. First, we carried out a Northwestern blot (NWB) assay by analyzing equal amounts of BSA, GST, recombinant purified APE1 wild-type (APE1^{WT}), as well as the tagged APE1^{WT}-GST protein (Fig. 2*A*). After gel running and blotting, we renatured the proteins by serial dilutions of GdnHCl, and then we incubated the membrane with the soluble fluorescent probe.

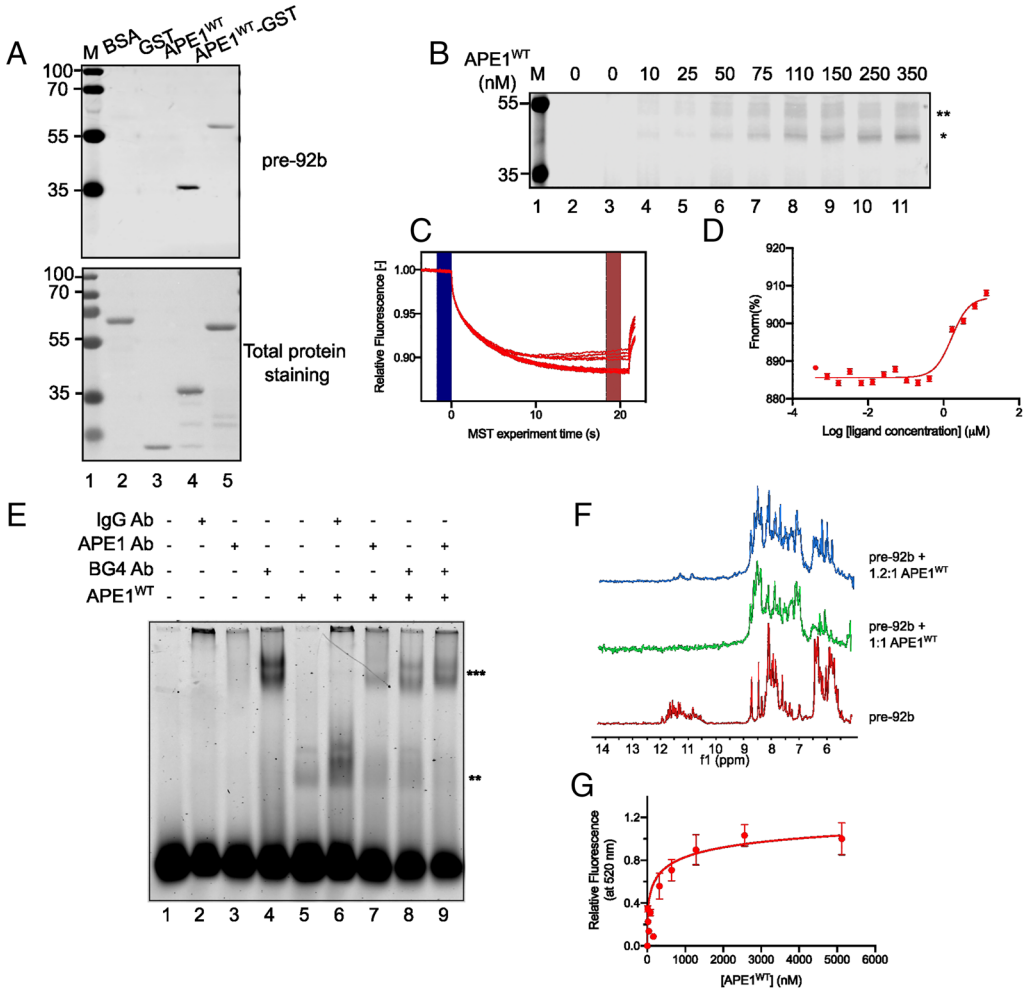

Fig. 2. APE1 binds pre-miR-92b rG4 and regulates its folding equilibrium. (*A*) Representative NWB shows the binding between pre-92b probe and the recombinant APE1^{WT} untagged (lane 4) and tagged with GST (APE1^{WT}-GST, lane 5). BSA and GST were used as controls (lanes 2 and 3). 1.5 μg of each protein was loaded on the SDS-PAGE gel and blotted on the membrane, as confirmed by the total protein staining. The membrane was incubated with the pre-92b fluorescent probe (5 pmol). On the left, the electrophoretic marker (M) is loaded (lane 1), and the different molecular weights are expressed in kDa. (*B*) Representative UV-cross-linking analysis with pre-92b probe (25 nM) and different amounts of APE1^{WT} reported upon the image and expressed in nM. On the left, the electrophoretic marker (M) is loaded and the different molecular weights are expressed in kDa. In lane 2, the oligoribonucleotide was heated at 70 °C before loading, as control. (*C*) Thermophoretic traces of the MST assay between pre-92b and APE1^{WT}, with the relative fluorescence [expressed in (–)] on the y-axis and the MTS experiment time on the x-axis (expressed in s). (*D*) Binding isotherm of the MST signals *versus* the logarithm of APE1^{WT} concentrations (μM). Experimental data derive from the average of two independent experiments. (*E*) Representative supershift REMSA gel with BG4 (lanes 4-8-9), IgG (lanes 2-6), APE1 (lanes 3-7-9) antibodies (215 nM), and recombinant APE1^{WT} (25 nM) (lanes from 5 to 9), incubated with a constant concentration of pre-92b probe (25 nM). pre-92b was heated at 70 °C before being added to the reactions. The asterisks (**) and (***) indicate the APE1-bound band and the antibodies-shifted bands, respectively. (*F*) 1D ^{1}H NMR spectra depicting 100 μM pre-92b in 10 mM KPi buffer with KCl and 0.5 mM $MgCl_2$. In red, the heterogenous folding pattern of different rG4 in a complex equilibrium. Green depicts the pre-92b after incubation with 1 molar equivalent of APE1. The blue spectrum shows the 1:1.2 molar ratio of protein to pre-92b. (*G*) Fluorescence study to monitor the structural conversion of an RNA duplex to an rG4 structure facilitated by recombinant APE1 protein. The APE1^{WT} concentration (expressed in nM) and the relative fluorescence at 520 nm are indicated on the x- and y-axis, respectively.

Data showed that both APE1^{WT} and APE1^{WT}-GST (lanes 4 and 5) were able to bind the probe. The absence of any bands in the BSA and GST lanes (lanes 2 and 3) confirmed that the binding of the probe to APE1^{WT} was highly specific. Moreover, to assess the specificity of the binding, we performed a NWB assay by comparing the signal obtained from pre-92b with a polyU RNA sequence of the same length as the pre-92b probe, as negative control. As shown in *SI Appendix*, Fig. S2*D*, a faint signal was observed with the polyU probe, as quantified and shown in the graph (*SI Appendix*, Fig. S2*E*), thus confirming the specificity of APE1^{WT} binding to the pre-92b probe. To further confirm these data, we carried out a UV-cross-linking assay using increasing amounts of APE1^{WT} protein and a constant amount of pre-92b probe (Fig. 2*B*). As indicated by the single asterisk, the observed band corresponded to the UV-cross-linked complex between APE1^{WT} and the pre-92b. Specifically, APE1^{WT} was able to bind the probe in a dose-dependent manner (lanes 4-11) forming a 1:1 ratio complex of 43 kDa. Some higher molecular complexes were also observed as faint bands and highlighted by double asterisks. As expected, not all these bands were detected in the protein-free oligoribonucleotide kept at room temperature (lane 3) nor in the protein-free oligoribonucleotide heated at 70 °C before loading (lane 2). To quantitatively evaluate the affinity between pre-92b probe and APE1^{WT}, we performed a MicroScale Thermophoresis (MST) assay (Fig. 2 *C* and *D*). Keeping the pre-92b probe concentration constant but increasing APE1^{WT} concentration, we obtained a dose–response profile and the fitting of the data allowed us to estimate an IC_{50} value of 1.6 ± 0.6 μM.

Since it was already known that APE1^{WT} facilitates the conversion of DNA-duplex structures to G4s (23), in order to characterize the possible involvement of APE1^{WT} in the folding process of rG4s, we performed a RNA electrophoretic mobility shift assay (REMSA) (40) with the recombinant purified protein (*SI Appendix*, Fig. S2*F*). In the presence of KCl and after favoring the probe denaturation by heating it at 70 °C, the unstructured probe

resulted in a single band (lane 1). After adding APE1^{WT}, multiple bands were observed (lanes 2-3-4, indicated by a single asterisk), whose intensity increased in an APE1^{WT}-dose-dependent manner. This result suggests that APE1^{WT} aids in shifting the equilibrium of the RNA toward a different structure, likely an rG4. Interestingly, the polyU probe was not shifted by APE1^{WT} (lanes 5 to 8), confirming the relevance of the RNA secondary structure for stable APE1^{WT} binding, as we previously observed in the case of DNA (45). The same assay was carried out by comparing the KCl buffer with the LiCl buffer (*SI Appendix*, Fig. S2*G*), which is known to destabilize G4 formation (46). The presence of APE1^{WT} increased the intensity of the retarded band in a dose-dependent manner, both in the KCl (lanes 2 and 3) or LiCl (lanes 5 and 6) buffer, but to a lower extent with the latter. Indeed, we observed a decrease of about 80% (*SI Appendix*, Fig. S2*H*), thus suggesting a competition effect between APE1^{WT} and LiCl in modulating the structural equilibrium of pre-92b rG4.

To further support the hypothesis that APE1^{WT} recognizes and modulates the structural equilibrium of pre-92b probe, a supershift-REMSA experiment was carried out (Fig. 2*E*). In this experiment, we specifically used BG4 antibody, which has been validated in literature for its binding ability toward DNA and RNA G-quadruplex structures (47), an APE1 antibody directed *versus* APE1^{WT} and an IgG antibody as a negative control. Again, pre-92b oligonucleotide was heated at 70 °C before being added to the different reactions. When the BG4 antibody was incubated alone with the pre-92b probe, a supershifted band was observed, suggesting that the folding of the rG4 occurs during the reaction incubation (lane 4). Epitope control IgG and APE1 antibodies were not able to shift the pre-92b probe (lanes 2 and 3, respectively), confirming the specificity of the BG4 antibody. APE1^{WT} alone was able to bind to the probe (lane 5) and the bound signal was increased when coincubated with IgG, although not shifted, as expected (lane 6). APE1 and BG4 antibodies were both able to supershift the APE1^{WT}-bound pre-92b probe, equally alone (lanes 7 and 8, respectively) and in combination (lane 9). Thanks to this experiment, and specifically to the BG4 antibody, we clearly showed that our pre-92b probe is folded to an rG4 in our REMSA, and that forms a complex with APE1^{WT} (lanes 7-8-9).

We then hypothesized the role of APE1^{WT} in modulating the folding equilibrium of the rG4 structure. We analyzed the structure of the complex between APE1^{WT} and the pre-92b probe by solution-state NMR spectroscopy (Fig. 2*F*). The 1D ^{1}H NMR spectrum of 100 μM pre-92b oligoribonucleotide in KPi buffer was recorded at 25 °C. The spectrum highlighted in red evidenced a complex imino peak pattern typical of rG4s. We could observe numerous imino peaks in the region of 10 to 12.5 ppm, indicating a heterogeneous folding pattern of different rG4s in a complex equilibrium. The green spectrum depicts the pre-92b probe incubated with one molar equivalent of APE1^{WT} for one hour before recording the same number of transients. The imino fingerprint vanished in the presence of APE1^{WT}, suggesting a potential unfolding of the rG4 into a single-stranded molecule, which can be in fast exchange with the water solvent and does not allow the formation of stable imino bonds among the nucleobases, as well as, the potential formation of higher-order aggregates. However, when we added pre-92b at a higher ratio (1:1.2 total molar ratio) to the NMR tube (blue spectrum), we observed the reappearance of some imino peaks, indicating a saturated level of the complex of APE1^{WT} with pre-92b at 1:1 interaction in which APE1^{WT} modulates the folding behavior of the rG4.

Finally, to understand whether APE1^{WT} could affect the folding of the possible rG4 sequence in pre-92b from a duplex-like RNA structure, we performed a fluorescence spectroscopy analysis (*SI Appendix*, Fig. S2*I* and Fig. 2*G*). To conduct this experiment, a 3′-FAM-labeled pre-92b probe was annealed with a complement bearing a 5′ quencher (BHQ), and the sequence provided the two natural bulges predicted in the pre-mir-92b structure (*SI Appendix*, Fig. S2*I*). The protein was titrated into the RNA solution while monitoring the evolution of the FAM fluorescence as the structure switched from duplex to rG4 (Fig. 2*G*). The experiment identified that APE1^{WT} could facilitate refolding of the duplex to an rG4 with a midpoint of 400 ± 90 nM (Fig. 2*G*) as happens for G4 in DNA (23).

In summary, our data confirm the hypothesis that APE1 can bind rG4-containing pre-miR-92b and modulate the folding equilibrium of its rG4 structure.

Lysine Residues within the APE1 N-Terminal Region are Required for Stable Binding to pre-miR-92b. Recent works from our laboratory showed that APE1 binding to G4, both in DNA promoters and telomeres, highly depends on its N-terminal region (23, 25). To deepen the role of this region in the recognition mechanism of the rG4 sequence, we performed in vitro assays using recombinant purified APE1^{WT}, together with APE1^{NΔ33} mutant protein, lacking the first 33 N-terminal residues, and APE1^{K4pleA} protein, a mutant in which lysine residues 27, 31, 32, and 35 are replaced by alanine residues to reset the positive charges of the lysine side chains (25). First, we performed a NWB assay (*SI Appendix*, Fig. S3*A* and Fig. 3*A*) by loading equal amounts of APE1^{WT}, APE1^{NΔ33}, and APE1^{K4pleA} recombinant proteins and BSA, as a negative control, as demonstrated by total protein staining (*SI Appendix*, Fig. S3*A*, *Bottom panel*). As expected, APE1^{WT}, APE1^{NΔ33,} and APE1^{K4pleA} were able to bind to pre-92b probe with different strengths (*SI Appendix*, Fig. S3*A*, *Upper panel*); indeed, the APE1^{NΔ33} quantified band was weaker than those of APE1^{WT} and APE1^{K4pleA} (Fig. 3*A*). Specifically, APE1^{NΔ33} lost 50% of its binding ability toward the pre-92b probe compared to APE1^{WT} (SD 0.13, $P \leq 0.001$), while APE1^{K4pleA} showed about a 32% decrease of its binding ability (SD 0.12, $P \leq 0.05$) (Fig. 3*A*).

Subsequently, as previously done for APE1^{WT}, we investigated whether APE1^{NΔ33} and APE1^{K4pleA} could form a stable rG4-containing pre-92b-protein complex. A UV-cross-linking assay was carried out using APE1^{NΔ33} and APE1^{K4pleA} in comparison with APE1^{WT} (Fig. 3*B* and *SI Appendix*, Fig. S3*B*). Differently from what observed for APE1^{WT}, the reactions between the probe and APE1^{NΔ33} or APE1^{K4pleA} provided very weak signals, both corresponding to the cross-linked adducts. Interestingly, APE1^{NΔ33} lost almost 80% of its rG4-binding ability, while the reduction observed in the case of APE1^{K4pleA} mutant was close to 50% (Fig. 3*B*).

To confirm these data, we conducted an MST assay by using all abovementioned APE1 proteins (Fig. 3*C* and *SI Appendix*, Fig. S3 *C* and *D*). The fitting of the dose-dependent signals provided an IC_{50} value of 2.8 ± 0.3 μM in the case of APE1^{NΔ33} mutant protein. Conversely, in the case of APE1^{K4pleA}, the fitting did not converge due to the lack of saturation values since this mutant exhibited limited water solubility with respect to the others. To deepen potential differences in the biophysical behaviors of APE1 recombinant proteins, we evaluated their CD spectra upon temperature increase. While APE1^{WT} and APE1^{NΔ33} exhibited a cooperative unfolding process providing similar T_m values (~44 °C) (*SI Appendix*, Fig. S3 *E* and *F*), we did not observe a cooperative mechanism, but rather the occurrence of aggregation upon temperature increase, in the case of APE1^{K4pleA} (*SI Appendix*, Fig. S3*G*). This aggregation propensity could explain the lower solubility. To better characterize APE1^{K4pleA} binding and structural equilibrium modulation toward pre-92b probe, we employed solution-state NMR spectroscopy (*SI Appendix*, Fig. S3*H*). As

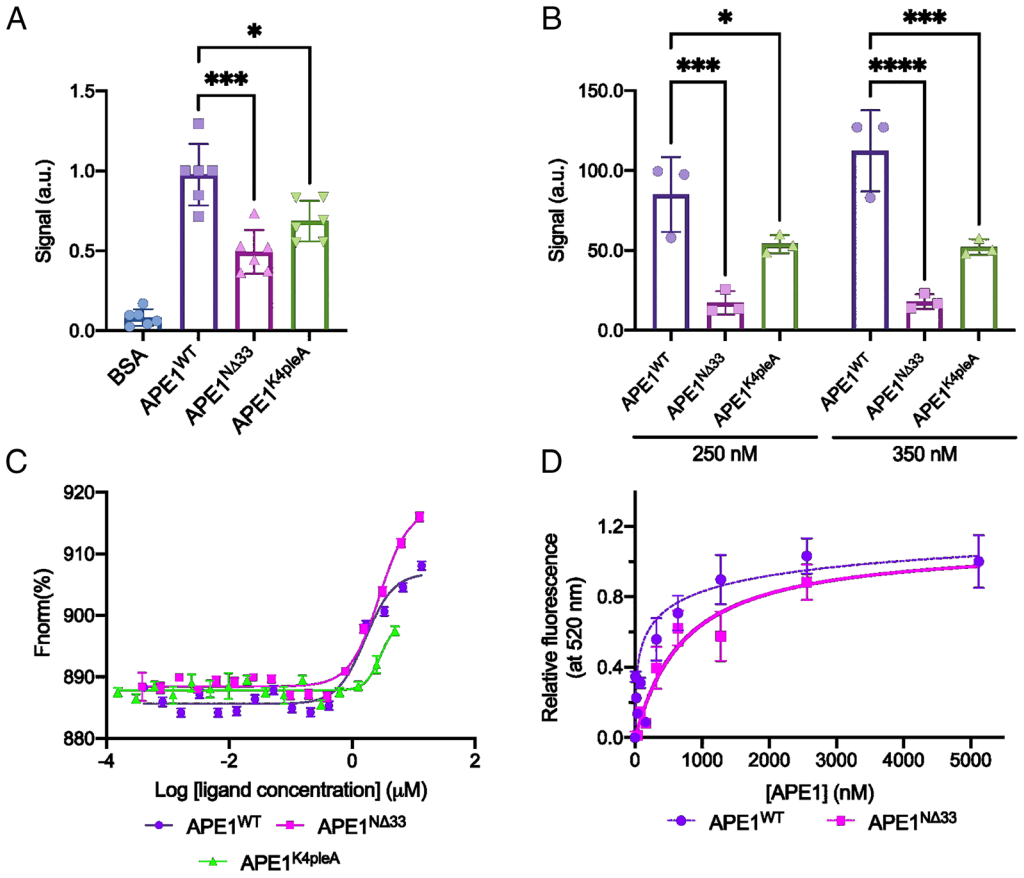

Fig. 3. APE1 N-terminal region is necessary for pre-miR-92b rG4 binding. (*A*) Histogram summarizing the different binding abilities obtained by NWB analysis toward pre-92b between BSA, APE1^{WT}, APE1$^{N\Delta33}$, and APE1^{K4pleA}, normalized on the respective total protein staining signal. The data are expressed as means ± SD of six independent replicates. (*B*) Histogram summarizing the different binding abilities obtained by UV-cross-linking analysis toward pre-92b between APE1^{WT}, APE1$^{N\Delta33}$, and APE1^{K4pleA}, at two different doses (250 and 350 nM). The data are expressed as means ± SD of three independent replicates. (*C*) Overlay of the isotherms of MST assays between pre-92b and the logarithm of APE1^{WT}, APE1$^{N\Delta33}$, and APE1^{K4pleA} concentrations (μM). The binding isotherm for the MST signal between pre-92b *versus* APE1^{WT}, APE1$^{N\Delta33}$, and APE1^{K4pleA} concentrations is reported. Experimental data derive from the average of two independent experiments. (*D*) Fluorescence study to monitor the structural conversion of an RNA duplex to an rG4 structure facilitated by recombinant APE1 and APE1$^{N\Delta33}$ proteins. The protein concentration (expressed in nM) and the relative fluorescence at 520 nm are indicated on the x- and y-axis, respectively. A *P*-value < 0.05 is symbolized by a single asterisk (*), while a *P*-value < 0.001 is symbolized by three asterisks (***) and <0.0001 by four asterisks (****).

shown in the 1D ^{1}H NMR spectrum (blue line), even in excess of APE1^{K4pleA} (1:1.2 total molar ratio), there was some remaining rG4 imino signature, indicating a weaker "unfolding" ability compared to APE1^{WT} (red line, 1:1 total molar ratio) and, indirectly, a lower binding affinity to the RNA, thus confirming NWB and UV-cross-linking results.

Finally, we used a fluorescence analysis to evaluate whether the N-terminal truncated mutant could regulate the rG4 folding from a duplex- structure, as happens for APE1^{WT}. The experiment, shown in Fig. 3*D*, demonstrated that APE1$^{N\Delta33}$ (pink line—780 ± 110 nM) could facilitate refolding to the rG4 at a twofold higher concentration than APE1^{WT} (purple line—400 ± 90 nM), demonstrating that the N-terminal region of the protein is necessary for the rG4 folding regulation of pre-92b probe.

Together, these data indicate that the N-terminal region of APE1 exerts a key role in the binding of the pre-92b and in the dynamic regulation of rG4 structures contained within.

APE1 Interacts with pre-miR-92b Sequence through its Canonical DNA Binding Interface. To investigate the interaction between APE1 and the pre-92b probe, we performed 2D NMR spectroscopy (*SI Appendix*, Fig. S4*A*). ^{15}N-^{1}H TROSY-HSQC experiments were performed using 60 μM of APE1 alone (green) and in the presence of 60 μM of pre-92b probe (red). As already observed in previous published NMR and X-ray crystallography experiments for the apo-APE1 (48) and APE1-DNA complex structures (49), the N-terminal region of the protein is not resolved due to highly flexible and intrinsically disordered amino acids. Nevertheless, using the 2D NMR spectra, we were able to follow important chemical shift modifications to key residues during the titration with pre-92b probe. In the apo form (green spectra), most residues were correctly identified, with aid from BMRB entry code 16516. Upon the addition of one molar equivalent of the pre-92b probe, prominent modifications in the spectrum occurred. Those chemical shift modifications were categorized into three groups: i) the first group, composed of residues that disappeared after the addition of RNA; ii) a second group that was not visible in the apo form while they appeared in the spectrum after RNA inclusion (red overlay spectra), and iii) the third group, which corresponded to visible peaks in the apo form that were shifted during the titration due to chemical shift changes. The disappearance of the residues can be explained by the extensive line broadening during the titration and as the result of a moderate affinity (μM range) between those amino acids and the RNA molecule that are usually in the range of intermediate exchange regime ($k_{ex} \approx |\Delta\omega|$). Between the disappearing residues localized in the canonical DNA binding region of APE1, we could find E216, T265, F266, M271, S307, and H309. For the second group, we detected the appearance of peaks at stoichiometric amounts, which led us to infer that the RNA molecule could induce conformational exchange processes.

Indeed, we observed peaks for residues localized in dynamic regions or undergoing conformational exchange, which were stabilized by interactions such as hydrogen bonds or salt bridges, often associated with specific binding. These peaks corresponded to amino acids directly involved in the ligand binding site, such as Y262 and M270. A few more peaks were observed but they could not be assigned unambiguously. We then plotted the disappearing and reappearing peaks, and the most significantly shifted peaks in the overlay of the apo (*SI Appendix*, Fig. S4*B*, peaks depicted in red) and the bound form (*SI Appendix*, Fig. S4*C*, peaks depicted in red) of APE1, with respective PDB accessing codes of 1BIX and 1DEW.

The structural representation allowed us to clearly identify the involvement of the helix–hairpin–helix (HhH) motif, which is responsible for recognizing and binding many DNA targets, including G4s (22).

Among the different amino acids that make part of the recognition and enzymatic site, apo-APE1 contains two important residues that were well conserved and undergo structural changes upon nucleic acid binding, e.g., R177 and M270 (cyan). These residues form a bridge-like structure that can be inserted into the major and minor grooves of RNA, respectively (purple for R177 and yellow for M270). Although we could not unambiguously identify R177 in the spectrum, M270 reappearance made us believe that APE1 binding toward the pre-92b probe is compatible with a classic binding mechanism observed in many other targets (50).

APE1 Regulates the Maturation and Shuttling of miR-92b in Cells with a High Prognostic Value in Real-World Cancers. We then evaluated the influence of APE1 on miR-92b maturation in human cancer cell lines. First, the ability of APE1 to bind either the precursor form of miR-92b, pri-miR-92b, or its mature form, miR-92b-3p, was investigated by RNA immunoprecipitation (RIP) (Fig. 4*A* and *SI Appendix*, Fig. S5 *A* and *B*) analysis in HeLa clones (27) including i) SCR, which expresses only the endogenous form of APE1; ii) cl.3, a doxycycline-inducible knock-down (KD) model for APE1 protein; and iii) $APE1^{WT}$ (WT) and iv) $APE1^{N\Delta33}$ (NΔ33) clones, expressing a Flag-tagged ectopic form of APE1 in place of the endogenous ones. The input and the FLAG-immunoprecipitated materials, upon RNA extraction procedure, were reverse-transcribed and analyzed by qPCR. Pri-miR-92b was successfully immunoprecipitated only in the WT clone whereas, as expected, no signal was obtained in both SCR and cl.3 clones (Fig. 4*A*). Furthermore, in accordance with the binding experiments, the NΔ33 clone lost about 80% of the immunoprecipitated pri-miR-92b compared to WT. We also investigated whether APE1 was able to bind miR-92b-3p, the most expressed strand of the two mature forms of pri-miR-92b (*SI Appendix*, Fig. S5*B*). Noteworthy, miR-92b-3p does not present any rG4-forming motif being cytosine-rich, and, in accordance, RIP analysis showed that the immunoprecipitated materials from the WT clone did not present any statistical enrichment of miR-92b-3p when compared to SCR and cl.3 clones. These results indicated that APE1 was able to bind rG4-containing pri-miR-92b also in the cellular context. As pri-miRNAs are prevalently double-stranded, these data would also suggest that the rG4-structure in pri-miR-92b could be in equilibrium with the double-stranded form.

In a previous publication, we demonstrated that cell depletion of APE1 led to an impairment of pri-miRNA processing for some specific miRNAs (27). For this reason, we examined whether APE1 was also involved in the maturation of pri-miR-92b. We checked pri-miR-92b and miR-92b-3p expression levels in the above-mentioned HeLa clones by qPCR (*SI Appendix*, Fig. S5 *C* and *D*). Specifically, pri-miR-92b levels were almost comparable between SCR and cl.3, with a slight decrease (15%) in the APE1-depleted clone, in line with what was previously described (27, 28). Furthermore, when APE1 expression was rescued by expression of siRNA-resistant ectopic $APE1^{WT}$ or $APE1^{N\Delta33}$ proteins, pri-miR-92b levels resulted comparable to the SCR. Moreover, we did not observe any significant changes in the levels of miR-92b-3p among the different clones (*SI Appendix*, Fig. S5*D*). These data indicate that APE1 is able to bind to the miR-92b precursor form, whereas its overall expression is only slightly influenced by APE1 depletion. Interestingly, recent works provided clear evidence of additional mechanisms of miRNA maturation and function by controlling their subcellular distribution and, in particular, the nuclear-cytoplasmic translocation (51). Specifically, nuclear miRNAs can regulate the biogenesis of other miRNAs or themselves by a regulatory feedback loop or directly targeting their primary transcripts in the nucleus. Moreover, nuclear miRNA localization has been associated with their targeting of nuclear-retained RNA transcripts, both coding and noncoding. Thus, we speculated that APE1 could influence and regulate the distribution of miRNAs between nuclei and cytosol. First, we evaluated the impact of APE1 depletion in the subcellular localization of miR-92b-3p by quantification through Fluorescence *In Situ* Hybridization (FISH) analysis in HeLa clones (*SI Appendix*, Fig. S6 and Fig. 4*B*). Under basal conditions (SCR), miR-92b-3p localization was both nuclear and cytosolic (red dots), being predominant in the nucleus. Upon APE1-KD (cl.3), miR-92b-3p was enriched in the nuclear compartment with the amount of nuclear miRNA significantly increased by about 43% compared to SCR, while its levels were significantly decreased in the cytosol by about 46% (Fig. 4*B*). When APE1 expression was rescued by the ectopic $APE1^{WT}$-Flag protein, the localization was comparable to SCR. Contrarily in the $APE1^{N\Delta33}$ rescue, we observed a higher number of red dots compared to SCR and WT clones, in both nuclear and cytosolic compartments, probably because $APE1^{N\Delta33}$ lacks its nuclear localization signal and is located in the cytosol. We confirmed FISH data by performing quantitative measurements through qPCR analyses on RNA obtained from nuclear and cytosolic compartment subfractionation. Thus, we isolated RNA and proteins from cytosolic and nuclear cell fractions from HeLa clones. First, we confirmed the efficiency of fractionation by performing a WB analysis (*SI Appendix*, Fig. S7*A*). Lamin A and tubulin antibodies were used as a control for the proper isolation of nuclei and cytosol, respectively. APE1 was prominently nuclear in SCR and WT clones, while predominantly cytoplasmic in NΔ33 clones, as expected. Afterward, we analyzed the levels of miR-92b-3p in the nuclear and cytoplasmic compartments by qPCR. In Fig. 4*C*, we showed that the APE1 depletion led to an accumulation of miR-92b-3p in the nucleus with a one-fold increase compared to SCR. The amount of cytoplasmic miR-92b-3p slightly decreased in APE1-depleted cells. Following the ectopic expression of $APE1^{WT}$-Flag, the localization of miR-92b-3p was almost comparable to what was observed in SCR. Finally, the rescue with the ectopic $APE1^{N\Delta33}$-Flag protein showed a similar trend of enrichment in the cytosol supporting the FISH results, although not statistically significant. Moreover, in support of our findings, we performed the same experiment by using stable APE1 knock-out (KO) clones derived from U2OS cells from osteosarcoma (52), that express a comparable level of miR-92b-3p than HeLa cells (*SI Appendix*, Fig. S7*B*). Upon fractioning of nuclear and cytosolic compartments of control cells and two different APE1 KO clones (KO1 and KO2) (*SI Appendix*, Fig. S7*C*), we observed that, also in this case, miR-92b-3p was significantly enriched in the nuclei of both KO clones compared to control (*SI Appendix*, Fig. S7*D*, blue bars). Again, no significant change was observed in the cytoplasmic compartment (brown bars).

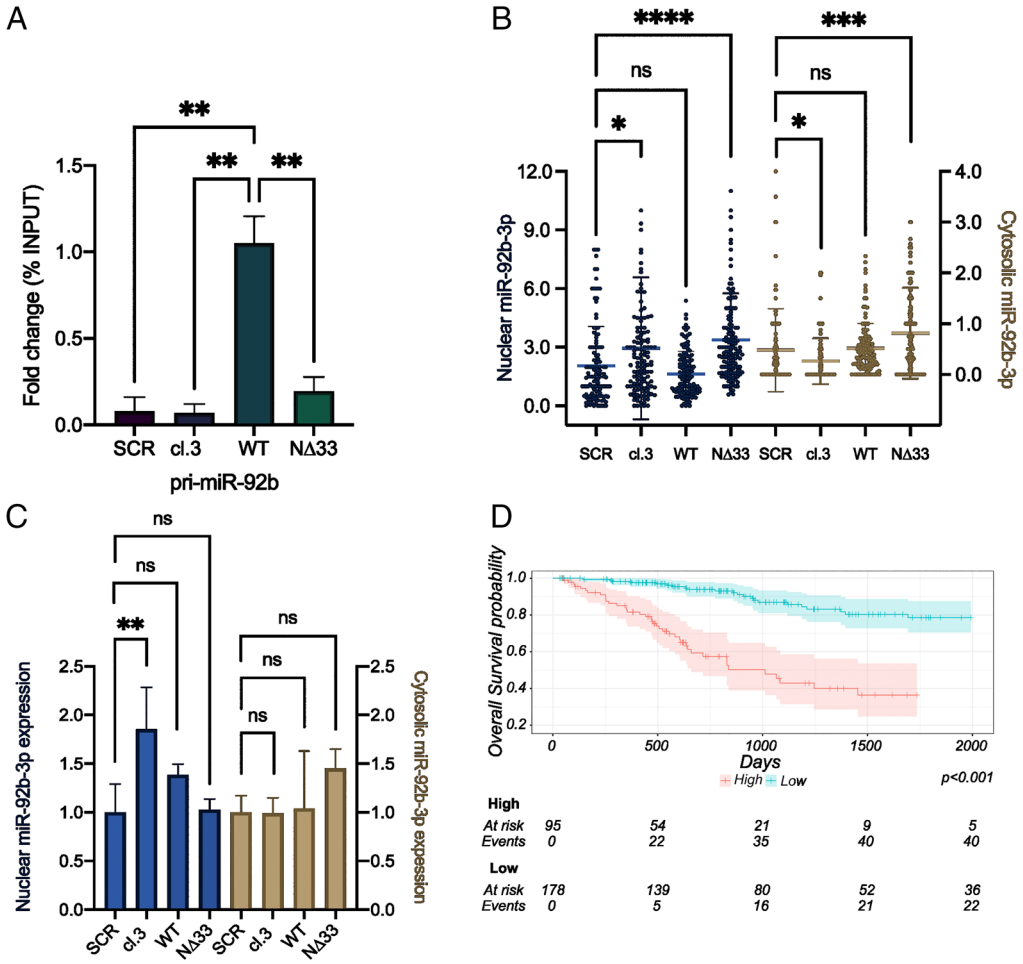

Fig. 4. APE1 binds pri-miR-92b in HeLa cells and influences the nucleo-cytosol localization of miR-92b-3p in HeLa cells. (*A*) Validation of APE1 binding toward pri-miR-92b in HeLa cell clones by RIP analysis. Data are represented as fold change percentage of the amount of immunoprecipitated target on the amount of the target present in the total input RNA (% INPUT) and normalized to APE1^{WT}. Data are expressed as means ± SD of two independent replicates. (*B*) Scatter plot of FISH analysis representing normalized individual values of miR-92b-3p in the nuclear (in blue) and cytoplasmic (in brown) compartment of HeLa clones silenced for endogenous APE1 expression. Nuclear and cytoplasmic miR-92b-3p dots were counted for each cell, using DAPI as a nuclear mask and APE1 as a cytoplasmic mask. The number of dots of miR-92b-3p was normalized on the number of dots of actin mRNA *per* each cell, in each compartment. The right axis corresponds to the nuclear miR-92b-3p levels, while the left one to the cytoplasmic miR-92b-3p levels. Data are expressed as means ± SD of two independent replicates. (*C*) The histogram shows the expression levels, measured by qRT-PCR, of miR-92b-3p in the nucleus, normalized on miR-484 and miR-196 levels, and the expression levels of miR-92b-3p in the cytoplasmic compartment, normalized to miR-16-5p levels in HeLa clones. Expression levels are normalized with respect to SCR. Data are expressed as means ± SD of three independent replicates. (*D*) Kaplan–Meier plots in the TCGA-CESC dataset show the different OS rates of subjects belonging to the "High risk" and "Low risk" groups, stratified based on the PI calculated from the miRNA signature. Results have been reported from 0 to 2,000 d, as sample size afterward is too small to perform statistical inference. A *P*-value < 0.05 is symbolized by a single asterisk (*), while a *P*-value < 0.01 is symbolized by two asterisks (**), < 0.001 by three asterisks (***), and < 0.0001 by four asterisks (****).

Overall, these data suggested that APE1 is involved in the maturation process and shuttling between the nucleus and cytoplasm of miR-92b, thus regulating its amount in both compartments.

Finally, to explore the prognostic power of rG4-miRNAs regulated by APE1 in different cancer types, we retrieved both miRNA expression and clinical data of TCGA samples for cervical squamous cell carcinoma and endocervical adenocarcinoma (TCGA-CESC), lung adenocarcinoma (TCGA-LUAD), and liver hepatocellular carcinoma (TCGA-LIHC). These specific tumor types were chosen to be consistent with cellular models used in this work and in our previous studies. For each dataset, we computed a Prognostic Index (PI) to stratify subjects into "High risk" and "Low risk" groups, based on both miRNA expression and association with overall survival (OS). In particular, the subject's PI was computed using multivariate Cox regression coefficients and the expression values of selected miRNAs for which expression data are available in the corresponding TCGA dataset (46 miRNAs in TCGA-LUAD and TCGA-CESC and 16 miRNAs in TCGA-LIHC). Subjects were then stratified into two groups, based on *P*-value optimization. Finally, Kaplan–Meier curves and a log-rank test were used to summarize data and compute the associated *P*-value. The OS rates were significantly different between the "High risk" and "Low risk" groups in all the analyzed datasets (TCGA-CESC, Fig. 4*D*, High risk = 95 and Low risk = 178, *P*-value = 5×10^{-14}, Hazard ratio Low risk/High risk = 0.17, TCGA-LUAD, *SI Appendix*, Fig. S8*A*, High risk = 142 and Low risk = 285, *P*-value = 1×10^{-12}, Hazard ratio Low risk/High risk = 0.33, TCGA-LIHC, *SI Appendix*, Fig. S8*B*, High risk = 118 and Low risk = 221, *P*-value = 3×10^{-8}, Hazard ratio Low risk/High risk = 0.37) suggesting that the expression of the miRNA signature is significantly associated with a different OS probability and supporting their potential prognostic value in the three analyzed cancer types. To identify the minimum miRNA signature associated with changes in the survival rate and to prioritize miRNAs based on their contribution, we then fitted a Cox regression model with LASSO penalization. The resulting LASSO lambda coefficients were used to rank miRNA based on their importance. In this case, miRNAs showing a coefficient equal to 0 have little to no impact on the signature and were thus excluded from the minimum signature. In particular, the minimum signature is

composed of the following miRNAs in the three datasets analyzed: in TCGA-CESC mir-642a, mir-1275, mir-1250, mir-1249, mir-296, mir-541, mir-320a, mir-1292, mir-1226, and mir-328 (*SI Appendix*, Fig. S8*C*), in TCGA-LUAD mir-1246, mir-3911, mir-320d-2, mir-92b, mir-328, mir-3940, mir-584, mir-1292, mir-940, mir-3195, mir-3187, mir-134, mir-1250, mir-541, mir-185, mir-642a, mir-200c, mir-615, mir-636, mir-9-1, mir-3928, mir-3615, mir-671, mir-877, mir-139b, and mir-675 (*SI Appendix*, Fig. S8*D*), and in TCGA-LIHC mir-1249, mir-3127, mir-197, mir-139, mir-1226, and mir-1250 (*SI Appendix*, Fig. S8*E*). Finally, to confirm the prognostic power of the minimum miRNA signature, we computed the PI using the LASSO lambda coefficients instead of the Cox coefficients. In this way, only miRNAs having a lambda coefficient different from 0 are considered. Subjects were then stratified into the "High risk" and "Low risk" groups based on *P*-value optimization, and a Kaplan–Meier curve along with a log-rank test was used to test the difference in the OS probability between the two groups. Interestingly, the minimum miRNA signature was still able to explain the difference in the OS probability between the two groups in all the analyzed datasets (TCGA-CESC, *SI Appendix*, Fig. S8*F*, High risk = 122 and Low risk = 151, *P*-value = 6×10^{-8}, Hazard ratio Low risk/High risk = 0.27, TCGA-LUAD, *SI Appendix*, Fig. S8*G*, High risk = 159 and Low risk = 268, *P*-value = 9×10^{-13}, Hazard ratio Low risk/High risk = 0.32, TCGA-LIHC, *SI Appendix*, Fig. S8*H*, High risk = 114 and Low risk = 225, *P*-value = 4×10^{-11}, Hazard ratio Low risk/High risk = 0.30).

These results, together with additional analysis on their target genes (*SI Appendix*, Fig. S9), supported the hypothesis that a major role of APE1 in tumor progression could be ascribable to its regulation of rG4-containing onco-miRNAs.

Discussion

rG4-containing miRNAs are recently emerging as dynamic post-transcriptional regulators of gene expression (53). Their folding and shuttling are controlled by RNA binding proteins (i.e., hnRNPA2B1, FUS, NCL, NPM1, etc.), RNA helicases (i.e., DHX36, hnRNP H/F), cations (i.e., Na^+ and K^+), and small molecules that are usually planar chromophores such as fused aromatic polycyclic systems, macrocycles, and nonfused aromatic systems with flexible structural motifs, making them highly dynamic (54). Recent data underline an emerging regulatory function played by rG4s in miRNA-maturation through Drosha and Dicer inhibition and a potential role in physiological and pathological liquid–liquid phase separation mechanisms (55, 56). In addition, several lines of evidence have shown that the presence of rG4s in pre-miRNAs is in equilibrium with the canonical stem-loop structure, and may regulate the maturation of some miRNAs, such as miR-63b, miR-1587, miR-26a-1, miR-1229, miR-3620-5p, pre-let-7, and miR-92b (15, 19, 57–59), thus offering a unique layer of gene expression regulation. Since dysregulation of miRNA biogenesis, as well as the quality control mechanisms of damaged miRNA processes, are emerging as hallmarks of cancer progression, it is essential to understand the regulatory aspects of these processes. In particular, defining the regulatory role of noncanonical structural elements, including rG4s, on miRNA function, maturation, shuttling, and processing would represent a step forward in translating these mechanisms into therapeutic opportunities for personalized medicine.

The literature has highlighted the importance of APE1 in gene expression regulation as well as the mediation of G4 structures in DNA (22, 26, 60). Indeed, through its redox domain, APE1 activates several TFs (32), by preferentially binding to G4 of several gene promoters, such as KRAS, NEIL3, and VEGF (22, 26, 60), and induces the formation of transcriptional hubs, enhancing gene expression. APE1 also regulates gene expression through post-transcriptional mechanisms involving miRNAs (21, 27, 32, 61). One example is represented by the expression of PTEN tumor suppressor, which is regulated by APE1 by two complementary mechanisms (27, 62). Indeed, APE1 activates the Egr-1 transcription factor through its redox domain, enhancing PTEN gene expression (62), while it also regulates miR-221/222 maturation, which post-transcriptionally targets PTEN, leading to its mRNA degradation (27). Given all these roles of APE1, the present study was conceived and designed to address the involvement of APE1 in the regulation of rG4-containing miRNAs.

In recent years, we aimed at the identification of those miRNAs whose expression is regulated by APE1 using different cancer cell lines (27, 28, 61). Surprisingly, among these miRNAs, we found that 27% contained an rG4 motif in their immature forms (Fig. 1*A*). We employed miR-92b as a model, for the reported role of the rG4 structure present in its precursor form (pre-miR-92b) in regulating its maturation (15, 19), and as it targets PTEN, whose expression, in turn, is regulated by APE1 at the transcriptional and post-transcriptional levels (27, 62). Here, we showed that APE1 is able to bind the pre-92b probe with a binding affinity in the low micromolar range, and dynamically regulate the rG4 structure within (Fig. 2). Binding experiments performed using Li^+ as counterion, which is known to disrupt G4 structures, are suggestive of an important role played by rG4-secondary structures as requirements for the stable binding by APE1 (*SI Appendix*, Fig. S2 *G* and *H*). However, additional experimental rigorous proof of this hypothesis should be reached. Moreover, another recent work by our laboratory supports our hypothesis that APE1 preferentially binds to rG4 (40). In this work, we characterized APE1's ability to bind miR-1246, which contains an EXO motif predicted to form an rG4 structure. Specifically, the use of a scrambled sequence in which the EXO motif was disrupted, led to a loss of APE1 binding ability. This finding reinforces our hypothesis that APE1 specifically binds to rG4 structures.

Of interest, we observed that the 33 N-terminal region of APE1 and, in particular, the lysine residues at position 27/31/32/35 are directly involved in the stabilization of the binding between APE1 and the rG4-containing pre-miR-92b (Fig. 3). These findings are in agreement with our previous evidence, underlining the relevance of these lysine residues in modulating the activity of APE1 on different RNA molecules (23, 25, 63). In addition, we showed that important flexible residues, such as the RM bridge and other residues located in the catalytic domain and the hydrophobic product pocket, are key players in the interaction with pre-92b probe (*SI Appendix*, Fig. S4).

Noticeably, FISH and qPCR cellular assays pointed out that APE1 cellular depletion causes miR-92b nuclear retention (Fig. 4) and these data are compatible with the general hypothesis that APE1, through its ability to modulate rG4 structures present in the precursor form of miR-92b, is involved in the maturation/shuttling process of the mature miR-92b, thus possibly contributing to miRNA biology and the post-transcriptional control of gene expression (64). Whether APE1 may act as a "simple chaperone" for rG4-containing miRNAs or take part in the enzymatic process involved in their maturation is currently unknown and should be further investigated.

Intriguingly, we observed that genes targeted by rG4-containing miRNAs, in turn, regulated by APE1, are associated with several pathways related to cancer onset and progression in the LUAD, CESC, and LIHC datasets (*SI Appendix*, Fig. S9). Besides

canonical cancer-related pathways like "small cell lung cancer" and "hepatocellular carcinoma," we also highlighted more specific pathways related to cell proliferation and apoptosis. Finally, it is also worth mentioning that pathways related to cell-to-cell and cell-to-extracellular matrix interactions are enriched with APE1-regulated miRNAs suggesting a role of APE1 in the EMT.

As previously described (32, 65–67), APE1 is overexpressed and serum-secreted in hepatocellular (HCC), NSCLC, and colon (CRC) cancers, representing a poor-outcome prognostic/predictive factor and an emerging anticancer target. Moreover, APE1 regulates onco-miRNA maturation and decay of oxidized- and abasic-miRNAs and can be secreted by cancer cells through extracellular vesicles (66, 68, 69). By analyzing TCGA datasets, we showed that the expression profile of rG4-containing miRNAs regulated by APE1 represents a promising tool to define a signature that clearly separates patients into two distinct groups characterized by a significant difference in the OS probability (Fig. 4*D* and *SI Appendix*, Fig. S8). This suggests the existence of a relationship between miRNA expression and survival in patients affected by lung, cervical, and hepatocellular cancers and confirms the important prognostic value of those miRNAs in the analyzed cancer types.

Herein, we provided evidence that a considerable number of APE1-regulated miRNAs (about 27%, Fig. 1*A*) contain putative rG4 structures which could be hypothesized to be directly bound and modulated by APE1, but some important questions still remain: i) which is the mechanism of regulation of rG4-free miRNAs; ii) how other rG4-containing miRNAs, not regulated by APE1, are controlled; iii) which is the role of APE1 protein partners (such as hnRNPA2B1 or FUS) in regulating its action, as recently shown for secreted miRNAs (40). Considering that i) rG4 structures present in immature miRNAs could hinder the processing activity of Dicer and other processing factors, thereby significantly affecting the miRNA maturation process (6), and ii) our current data showing that APE1 cellular depletion leads to nuclear retention of miR-92b, it is possible that the lack of a significant enrichment of rG4-containing miRNAs among those dysregulated by APE1 (Fig. 1) may be due to missing information in the datasets currently available in our laboratory. Indeed, these datasets were obtained as deregulated miRNAs upon APE1 silencing starting from total cell extracts, without employing any specific cellular subfractionation procedures. For this reason, to address this issue, we believe that the next efforts should be focused on the identification of those miRNAs that are dysregulated in the nuclear and cytosolic compartments upon APE1 depletion to possibly better highlight the enrichment of rG4-containing miRNAs. As of now, work is ongoing in our laboratory to address this point. Furthermore, several RNA helicases and additional RBPs, including some recognized as APE1 interactors, are able to control a distinct subset of rG4 (7). This suggests that specific combinations of RBP/RNA helicases may regulate different subsets of rG4s, supporting our findings that APE1 could not be the only regulator of rG4-containing miRNA, but highlights the potential existence of distinct "regulons."

Overall, we believe that this study paves the way for unique perspectives in understanding the role of this unconventional DNA repair protein in the regulation of gene expression and that additional future studies should appropriately address.

As recently proposed (39), after genotoxic treatment, damaged miRNAs including those containing AP or 8-oxoG sites, seem to accumulate up to 10-fold or more in cells, having fundamental effects on gene expression (70), and an important epitranscriptional regulation on cancer development. Whereas, in duplex DNA, the electron holes can travel over long distances (from 100 s to 1000s bp) until reaching a GGG site (as found in G4 motifs) with a low redox potential site, thus forming an 8-oxoG, in the case of RNA, this does not happen to the same extent. Currently, the frequency of AP and 8-oxoG sites in miRNAs is still unknown. It is plausible that guanine oxidation may rewire miRNAs by differentially regulating redox-dependent cancer development as well as the modulation of miRNA processing and decay during genotoxic stress may be part of the executive mechanism of chemoresistance (39). Not least, the biochemical mechanisms responsible for the repair of oxidized bases and the generation of AP sites in miRNAs remain unknown. On these topics, the ability of APE1 to recognize and process miRNAs containing both AP and 8-oxoG sites, alone or in combination with additional proteins such as hnRNPD (71) or PCBP1 (72), may represent an interesting subject of investigation focused on defining the regulatory functions of rG4s present in several miRNAs (39, 70), and for understanding the molecular mechanisms of miRNA quality control with the ultimate goal of developing eligible specific anticancer strategies. Future work in our laboratory will be devoted to addressing these issues.

Materials and Methods

Bioinformatic rG4 Prediction, Functional Enrichment, and Network miRNA–Gene Analysis. We examined the presence of rG4-forming motif sequences in the pre-miRNAs through a bioinformatic analysis using three algorithms, namely QGRS mapper [score threshold = 19, (73)], pqsfinder [score threshold = 47, (74)] and G4Hunter [score threshold = 1,2, (75)].

To identify deregulated pathways associated with APE1 KD, we have performed an enrichment analysis using ClusterProfiler by querying the KEGG database (76) on the union of up-regulated genes from HeLa and A549 cells (q-value < 0.05). In order to decipher the regulatory miRNA–gene network of the 61 miRNA signature, we retrieved the associated target genes from TarBase. For further detailed information, refer to *SI Appendix*.

Synthetic Oligoribonucleotides. For NWB, REMSA, UV-cross-linking, and MST analysis, we used a twenty-nucleotide long oligoribonucleotide with the following sequence 5′-CCGGGCGGGCGGGAGGGACG-3′. For CD analysis and fluorescence spectroscopy, the oligoribonucleotide sequence was 5′-CCGGGCGGGCGGGAGGGAC-3′. In all experiments, these oligoribonucleotides were indicated as pre-92b. For further detailed information regarding the synthesis and annealing, refer to *SI Appendix*.

Expression of Recombinant Proteins and FPLC Purification. Expression of human recombinant GST-tagged and untagged APE1^{WT}, APE1$^{N\Delta 33}$, and APE1^{K4pleA} proteins was obtained as explained in ref. 25.

SDS-PAGE, Western Blotting (WB), and Northwestern Blot (NWB) Analysis. SDS-PAGE and WB were conducted as explained in ref. 27. The primary antibodies used and their dilution were the following: APE1 (NB 100-116, mouse, monoclonal, 1:2,000, Novus); β-tubulin (T 0198, mouse, monoclonal, 1:2,000, Merck); and lamin-A (ab8980, mouse, monoclonal, 1:1000, Abcam).

The NWB assay was performed as explained in ref. 71 and incubated with 5 pmol of the labeled oligoribonucleotides. After washing, the membranes were scanned by an Odyssey CLx scanner and analyzed by ImageStudio Software (Li-Cor Biosciences).

REMSA and UV-Cross-Linking Analysis. RNA Electrophoretic Mobility Shift (REMSA) reactions were prepared in a final volume of 20 μl, by incubating the indicated doses of APE1 recombinant protein with 25 nM of the oligoribonucleotides. The oligoribonucleotides were heated at 70 °C before being added to the reaction, which was carried out in rG4 buffer containing 20 mM Tris-HCl pH 7.4, 100 mM KCl, 0.5 μg/μl BSA, and 0.25% glycerol. For the supershift REMSA, the following primary antibodies (215 nM) were used: BG4 (MABE1126, mouse, monoclonal, Merck); APE1 (NB 100-101, rabbit, polyclonal, Novus); and IgG (sc-69917, rat, monoclonal, Santa Cruz Biotechnology). The reactions were incubated for 20 min at RT and then added with 2 μl of Orange Loading Dye (Li-Cor Biosciences). The samples were then run on a 4% or on a 15% native PAGE gel at 60 V for the first 15 min and then increasing at 80 V for the remaining 60 or 100 min (respectively, for the 4% and 15% gel) at 4 °C in TBE 0.5 X.

For the UV-cross-linking analysis, the reactions were prepared in a final volume of 20 μl with the indicated doses of APE1 recombinant protein and 25 nM of the oligoribonucleotide, in rG4 buffer. The reactions were incubated for 30 min at 4 °C and then UV-cross-linked at 0.2 J/m^2. The samples were then added with Laemmli 4X and heated at 95 °C for 5 min. The samples were run on a 12% SDS-PAGE gel.

After running, REMSA and UV-cross-linking gels were scanned by an Odyssey CLx scanner and analyzed by ImageStudio Software (Li-Cor Biosciences).

MicroScale Thermophoresis (MST) Experiments. MST experiments were carried out with a Monolith NT 115 system (Nano Temper Technologies) equipped with 20% LED and 40% IR-laser power. For the assay, a 16-step serial dilution (1:1) procedure was performed, with the final concentrations of 12.5 μM for $APE1^{WT}$, 13.5 μMfor $APE1^{NΔ33}$, and 5 μM for $APE1^{K4pleA}$; pre-92b probe was added in each tube at a final concentration of 625 nM. The samples were filled into standard capillaries, and measurements were carried out at 25 °C in a buffer containing 25 mM Tris-HCl pH 7.5, 100 mM NaCl, 50 mM KCl, and 1 mM DTT. Experimental data derive from the average of two separate experiments. The equation, used for fitting data at different concentrations, was implemented by the Prism GraphPad 7.0 software with the equation nonlinear regression log (inhibitor) vs. response (three parameters).

Circular Dichroism (CD) Analysis and UV and Fluorescence Spectroscopies. CD experiments and UV and fluorescence spectroscopies were conducted as explained in ref. 23. For additional information, refer to *SI Appendix*.

Cell Culture and Compounds. HeLa cells and stable clones were grown as indicated in ref. 27. U2OS cell clones were grown as indicated in ref. 52.

RNA Extraction and Quantitative Real-Time PCR (qRT-PCR). For the separation of nuclear and cytosolic RNA, we followed the protocol in ref. 77. Total, nuclear, and cytosolic RNA pellets were resuspended in Qiazol, and RNA was extracted using the miRNeasy kit (Qiagen), according to the manufacturer's instructions. For qRT-PCR information, refer to *SI Appendix*.

RNA Immunoprecipitation (RIP) Analysis. RIP analysis on HeLa cell clones was performed as previously described in ref. 27.

Fluorescence In Situ Hybridization (FISH) analysis. HeLa cell clones, treated with doxycycline for 10 d (27), were seeded ontocoverslips in 24-multiwell and allowed to grow to 60–80% confluency. Coverslips were stained using the ViewRNA™ Cell Plus Assay Kit (ThermoFisher), according to the manufacturer's instructions. The detection of the targets was carried out using miR-92b-3p Type 1 probe (VM1-10117-01, ThermoFisher), miR-16-5p Type 1 probe (VM1-10232-01, ThermoFisher), and ACTB, human Type 4 probe (VA4-10293-01, ThermoFisher). APE1 was stained by using anti-APE1 antibody (NB 100-116, mouse, monoclonal, 1:100, Novus) and Alexa® 633 secondary antibody (A211050, mouse, polyclonal, 1:100, Invitrogen). All images were captured by confocal microscopy (Leica) in z-stack. Maximum projections were analyzed using ImageJ software.

NMR Titration. Both 1D and 2D NMR experiments were recorded on a Bruker Advance III 700 and 800 MHz spectrometer equipped with a liquid TXI 1H/13C/15 N/2H probe. Samples (3 mm NMR tubes) were prepared in Kpi buffer 10 mM K_2HPO_4/KH_2PO_4, 50 mM KCl, 2 mM $MgCl_2$, and 0.2 mM TCEP at pH 6.8. D_2O (8%) was used as reference. APE1 was used at 100 (1D) or 64 (2D) μM. In the 1D ^{1}H NMR experiments, the water signal was suppressed using excitation sculpting with gradients (zgesgppe; d1=2 s; 512 scans; time domain=64 k). We used Transverse Relaxation-Optimized Spectroscopy (TROSY) to acquire the 2D titration spectra. Each residue has been identified by the −NH from its backbone connection and assigned using the deposited data from PDB structure 1BIX and 1DEW together with data available at the BMRB entry 16516. NMR data were treated using TopSpin 4.1, NMRFAM-Sparky (Bruker Biospin) (78), and the structure analysis was performed with UCSF Chimera (79). For the representation of chemical shift variations, we only considered peaks that were unambiguously identified, and they were mapped on the surface of $APE1^{WT}$. The following criteria were used: The addition of RNA to the NMR tube containing $APE1^{WT}$ led to a decrease of intensity for several peaks, while some peaks completely vanished, such as those corresponding to W67, Y87, T97, R177, R181, L182, F232, T265, C310, and I312. Other peaks were shifted, such as (in ppm values), V69 (0.5), L72 (0.05), K98 (0.05), Gly147 (0.12) D216 (0.23), N226 (0.35), M271 (0.07), and K273 (0.03).

Survival Analysis. The prognostic value of selected miRNAs was evaluated in three datasets retrieved from The Cancer Genome Atlas (TCGA) including Lung Adenocarcinoma (TCGA-LUAD), Cervical Squamous Cell Carcinoma, and Endocervical Adenocarcinoma (TCGA-CESC), and Liver Hepatocellular Carcinoma (TCGA-LIHC). For further detailed information, refer to *SI Appendix*.

Statistical Analysis. The results are presented as means ± SD, and data analysis was performed with the Prism GraphPad 7.0 software. For comparisons between multiple groups, ordinary one-way ANOVA was used. In all tests, adjusted P-values < 0.05 were considered statistically significant. *$P \le 0.05$; **$P \le 0.01$; ***$P \le 0.001$; ****$P \le 0.0001$.

Data, Materials, and Software Availability. Raw Data have been deposited in Open Science Framework (OSF) (https://osf.io/jch3g/?view_only=4639cd6e2ed3447c9c7cc3496392ee83) (80). All study data are included in the article and/or supporting information.

ACKNOWLEDGMENTS. The work was supported by Associazione Italiana per la Ricerca sul Cancro (AIRC) with Grant number IG19862 to G.T. and Grant IG27378 to D.M., through the support of the Departmental Strategic Plan (PSD) of the University of Udine-Interdepartmental Project on AI (2020-25), and by additional Grants from the University of Udine ("Bando Ricerca Collaborativa" granted by European Community - NextGenerationEU) and from the Consorzio Interuniversitario Biotecnologie–C.I.B.–(MUR-PRIN2022: "L'INNOVAZIONE DELLE BIOTECNOLOGIE NELL'ERA DELLA MEDICINA DI PRECISIONE, DEI CAMBIAMENTI CLIMATICI E DELL'ECONOMIA CIRCOLARE") to G.T. This work was also partly supported by a grant from MUR-PRIN2022 (grant#20224F7P9Y) to G.T. and by a private donation by Mr. Di Giusto to G.T. We especially thank Stokasimov E. from Pellman Lab (Cell Division and Genome Instability), Boston Children's Hospital, for the U2OS KO cell model. Moreover, C.J.B. and A.F.M. thank the U.S. NIH via R35 GM145237 for financial support. Z.O. is recipient of Excellence Eiffel fellowship from The French "Ministère de l'Europe et des Affaires Étrangères". We appreciate the effort from Brune Vialet for the synthesis of oligonucleotides under short notice. Finally, G.S. thanks the IR INFRANALYTICS FR2054 and the IECB NMR platform at the University of Bordeaux.

Author affiliations: [a]Laboratory of Molecular Biology and DNA repair, Department of Medicine, University of Udine, Udine 33100, Italy; [b]Liver Cancer Unit, Fondazione Italiana Fegato—Organizzazione Non Lucrativa di Utilità Sociale, Basovizza 34149, Italy; [c]Department of Life Sciences and Technology for Health, ARNA laboratory, INSERM U1212, CNRS, UMR 5320, University of Bordeaux, Bordeaux F-33076, France; [d]Department of Chemistry, University of Utah, Salt Lake City, UT 84112-0850; [e]STARS lab (Structure Activity Relationship Synthesis and Spectroscopy), Department of Pharmacy, University of Naples "Federico II", Naples 80131, Italy; and [f]Laboratory of RNA Regulatory Networks, Department of Cellular, Computational and Integrative Biology, University of Trento, Trento 38123, Italy

Author contributions: G.T. designed research; A.B., M.C.M., G.S., A.M.F., Z.O., S.L.M., and D.M. performed research; A.B., M.C.M., G.S., A.M.F., G.A., Z.O., N.G., S.L.M., D.M., E.D., C.J.B., and G.T. analyzed data; and A.B., M.C.M., G.S., A.M.F., N.G., S.L.M., D.M., E.D., C.J.B., and G.T. wrote the paper.

1. B. Baptista, M. Riscado, J. A. Queiroz, C. Pichon, F. Sousa, Non-coding RNAs: Emerging from the discovery to therapeutic applications. *Biochem. Pharmacol.* **189**, 114469 (2021).
2. S. Ghafouri-Fard, H. Shoorei, F. T. Anamag, M. Taheri, The role of non-coding RNAs in controlling cell cycle related proteins in cancer cells. *Front. Oncol.* **10**, 608975 (2020).
3. L. L. Yan, H. S. Zaher, How do cells cope with RNA damage and its consequences? *J. Biol. Chem.* **294**, 15158–15171 (2019).
4. J. O'Brien, H. Hayder, Y. Zayed, C. Peng, Overview of MicroRNA biogenesis, mechanisms of actions, and circulation. *Front. Endocrinol.* **9**, 402 (2018).
5. H. A. Meijer, E. M. Smith, M. Bushell, Regulation of miRNA strand selection: Follow the leader? *Biochem. Soc. Trans.* **42**, 1135–1140 (2014).
6. F. Li, J. Zhou, G-quadruplexes from non-coding RNAs. *J. Mol. Med. (Berl)* **101**, 621–635 (2023).
7. L. Dumas, P. Herviou, E. Dassi, A. Cammas, S. Millevoi, G-quadruplexes in RNA biology: Recent advances and future directions. *Trends in Biochem. Sci.* **46**, 270–283 (2021).
8. P. Agarwala, S. Pandey, S. Maiti, The tale of RNA G-quadruplex. *Organic Biomol. Chem.* **13**, 5570–5585 (2015).

9. M. Zhu *et al.*, Novel roles of an intragenic G-quadruplex in controlling microRNA expression and cardiac function. *Nucleic Acids Res.* **49**, 2522–2536 (2021).
10. S. G. Rouleau, J.-M. Garant, F. Bolduc, M. Bisaillon, J.-P. Perreault, G-Quadruplexes influence pri-microRNA processing. *RNA Biol.* **15**, 198–206 (2018).
11. J. Figueiredo *et al.*, Targeting nucleolin by RNA G-quadruplex-forming motif. *Biochem. Pharmacol.* **189**, 114418 (2021).
12. K. L. Chan *et al.*, Structural analysis reveals the formation and role of RNA G-quadruplex structures in human mature microRNAs. *Chem. Commun.* **54**, 10878–10881 (2018).
13. I. Slezak-Prochazka, S. Durmus, B.-J. Kroesen, A. van den Berg, MicroRNAs, macrocontrol: Regulation of miRNA processing. *RNA* **16**, 1087–1095 (2010).
14. K. Lyu, E.Y.-C. Chow, X. Mou, T.-F. Chan, C. K. Kwok, RNA G-quadruplexes (rG4s): Genomics and biological functions. *Nucleic Acids Res.* **49**, 5426–5450 (2021).
15. G. Mirihana Arachchilage, A. C. Dassanayake, S. Basu, A potassium ion-dependent RNA structural switch regulates human pre-miRNA 92b maturation. *Chem. Biol.* **22**, 262–272 (2015).
16. H. Song *et al.*, miR-92b regulates glioma cells proliferation, migration, invasion, and apoptosis via PTEN/Akt signaling pathway. *J. Physiol. Biochem.* **72**, 201–211 (2016).
17. J.-H. Guo *et al.*, MicroRNA-92b acts as an oncogene by targeting PTEN/AKT in NSCLC. *Cell Biochem. Funct.* **38**, 1100–1110 (2020).
18. Y. Li *et al.*, MiR-92b regulates the cell growth, cisplatin chemosensitivity of A549 non small cell lung cancer cell line and target PTEN. *Biochem. Biophys. Res. Commun.* **440**, 604–610 (2013).
19. G. Mirihana Arachchilage, P. Kharel, J. Reid, S. Basu, Targeting of G-quadruplex harboring pre-miRNA 92b by LNA rescues PTEN expression in NSCL cancer cells. *ACS Chem. Biol.* **13**, 909–914 (2018).
20. M. C. Malfatti *et al.*, New perspectives in cancer biology from a study of canonical and non-canonical functions of base excision repair proteins with a focus on early steps. *Mutagenesis* **35**, 129–149 (2020).
21. M. C. Malfatti, G. Antoniali, M. Codrich, G. Tell, Coping with RNA damage with a focus on APE1, a BER enzyme at the crossroad between DNA damage repair and RNA processing/decay. *DNA Repair* **104**, 103133 (2021).
22. S. Pramanik *et al.*, The human AP-endonuclease 1 (APE1) is a DNA G-quadruplex structure binding protein and regulates KRAS expression in pancreatic ductal adenocarcinoma cells. *Nucleic Acids Res.* **50**, 3394–3412 (2022).
23. A. M. Fleming, S. A. H. Manage, C. J. Burrows, Binding of AP endonuclease-1 to G-quadruplex DNA depends on the N-terminal domain, Mg2+ and ionic strength *ACS Bio. Med. Chem. Au.* **1**, 44–56 (2021).
24. A. M. Fleming, Y. Ding, C. J. Burrows, Oxidative DNA damage is epigenetic by regulating gene transcription via base excision repair. *Proc. Natl. Acad. Sci. U.S.A.* **114**, 2604–2609 (2017).
25. S. Burra *et al.*, Human AP-endonuclease (Ape1) activity on telomeric G4 structures is modulated by acetylatable lysine residues in the N-terminal sequence. *DNA repair* **73**, 129 (2019).
26. S. A. Howpay Manage, J. Zhu, A. M. Fleming, C. J. Burrows, Promoters vs. telomeres: AP-endonuclease 1 interactions with abasic sites in G-quadruplex folds depend on topolog. *RSC Chem. Biol.* **4**, 261–270 (2023).
27. G. Antoniali *et al.*, Mammalian APE1 controls miRNA processing and its interactome is linked to cancer RNA metabolism. *Nat. Commun.* **8**, 797 (2017).
28. G. Antoniali *et al.*, APE1 controls DICER1 expression in NSCLC through miR-33a and miR-130b. *Cell Mol. Life Sci.* **79**, 446 (2022).
29. Z. Sun *et al.*, Differential expression of APE1 in hepatocellular carcinoma and the effects on proliferation and apoptosis of cancer cells. *Biosci. Trends* **12**, 456–462 (2018).
30. X. Yang *et al.*, The regulatory role of APE1 in epithelial-to-mesenchymal transition and in determining EGFR-TKI responsiveness in non-small-cell lung cancer. *Cancer Med.* **7**, 4406–4419 (2018).
31. D. Lou, L. Zhu, H. Ding, H.-Y. Dai, G.-M. Zou, Aberrant expression of redox protein Ape1 in colon cancer stem cells. *Oncol. Lett.* **7**, 1078–1082 (2014).
32. M. C. Malfatti, A. Bellina, G. Antoniali, G. Tell, Revisiting two decades of research focused on targeting APE1 for cancer therapy: The pros and cons. *Cells* **12**, 1895 (2023).
33. J. Vohhodina, D. P. Harkin, K. I. Savage, Dual roles of DNA repair enzymes in RNA biology/post-transcriptional control. *Wiley Interdiscip Rev. RNA* **7**, 604–619 (2016).
34. L. Jobert, H. Nilsen, Regulatory mechanisms of RNA function: Emerging roles of DNA repair enzymes. *Cell Mol. Life Sci.* **71**, 2451–2465 (2014).
35. C. L. Simms, H. S. Zaher, Quality control of chemically damaged RNA. *Cell. Mol. Life Sci.* **73**, 3639–3653 (2016).
36. V. O. Wickramasinghe, A. R. Venkitaraman, RNA processing and genome stability: Cause and consequence. *Mol. Cell* **61**, 496–505 (2016).
37. M. Tanaka, P. B. Chock, E. R. Stadtman, Oxidized messenger RNA induces translation errors. *roc. Natl. Acad. Sci. U.S.A.* **104**, 66–71 (2007).
38. A. Calabretta, P. A. Küpfer, C. J. Leumann, The effect of RNA base lesions on mRNA translation. *Nucleic Acids Res.* **43**, 4713–4720 (2015).
39. S. Eom *et al.*, Widespread 8-oxoguanine modifications of miRNA seeds differentially regulate redox-dependent cancer development. *Nat. Cell Biol.* **25**, 1369–1383 (2023).
40. G. Mangiapane *et al.*, The DNA-repair protein APE1 participates with hnRNPA2B1 to motif-enriched and prognostic miRNA secretion. *Oncogene* **43**, 1861–1876 (2024).
41. A. Kozomara, M. Birgaoanu, S. Griffiths-Jones, miRBase: From microRNA sequences to function. *Nucleic Acids Research* **47**, D155–D162 (2019).
42. D. Karagkouni *et al.*, DIANA-TarBase v8: A decade-long collection of experimentally supported miRNA-gene interactions. *Nucleic Acids Res.* **46**, D239–D245 (2018).
43. C. Wu, Focal adhesion: A focal point in current cell biology and molecular medicine. *Cell Adh Migr* **1**, 13–18 (2007).
44. R. Del Villar-Guerra, J. O. Trent, J. B. Chaires, G-quadruplex secondary structure obtained from circular dichroism spectroscopy. *Angew. Chem. Int. Ed. Engl.* **57**, 7171–7175 (2018).
45. M. Poletto *et al.*, Role of the unstructured N-terminal domain of the hAPE1 (human apurinic/apyrimidinic endonuclease 1) in the modulation of its interaction with nucleic acids and NPM1 (nucleophosmin). *Biochem. J.* **452**, 545–557 (2013).
46. D. Bhattacharyya, G. Mirihana Arachchilage, S. Basu, Metal cations in G-quadruplex folding and stability. *Front. Chem.* **4**, 38 (2016).
47. G. Biffi, M. Di Antonio, D. Tannahill, S. Balasubramanian, Visualization and selective chemical targeting of RNA G-quadruplex structures in the cytoplasm of human cells. *Nat. Chem.* **6**, 75–80 (2014).
48. M. A. Gorman *et al.*, The crystal structure of the human DNA repair endonuclease HAP1 suggests the recognition of extra-helical deoxyribose at DNA abasic sites. *EMBO J.* **16**, 6548–6558 (1997).
49. C. D. Mol, T. Izumi, S. Mitra, J. A. Tainer, DNA-bound structures and mutants reveal abasic DNA binding by APE1 and DNA repair coordination [corrected]. *Nature* **403**, 451–456 (2000).
50. T.-C. Liu *et al.*, APE1 distinguishes DNA substrates in exonucleolytic cleavage by induced space-filling. *Nat. Commun.* **12**, 601 (2021).
51. X. Hu *et al.*, Recent advances in the functional explorations of nuclear microRNAs. *Front. Immunol.* **14**, 1097491 (2023).
52. S. Tang, E. Stokasimov, Y. Cui, D. Pellman, Breakage of cytoplasmic chromosomes by pathological DNA base excision repair. *Nature* **606**, 930–936 (2022).
53. D. Varshney, J. Spiegel, K. Zyner, D. Tannahill, S. Balasubramanian, The regulation and functions of DNA and RNA G-quadruplexes. *Nat. Rev. Mol. Cell Biol.* **21**, 459–474 (2020).
54. S. Ghafouri-Fard *et al.*, Interaction between non-coding RNAs, mRNAs and G-quadruplexes. *Cancer Cell Int.* **22**, 171 (2022).
55. S. Asamitsu, N. Shioda, Potential roles of G-quadruplex structures in RNA granules for physiological and pathological phase separation. *J. Biochem.* **169**, 527–533 (2021).
56. Y. Zhang *et al.*, G-quadruplex structures trigger RNA phase separation. *Nucleic Acids Res.* **47**, 11746–11754 (2019).
57. K. Lyu, C. K. Kwok, A G-quadruplex structure in microRNA interferes with messenger RNA recognition and controls gene expression. *Chem. Commun. (Camb)* **59**, 8230–8233 (2023).
58. F. Li *et al.*, G-quadruplex from precursor miR-1587 modulated its maturation and function. *Int. J. Biol. Macromol.* **231**, 123279 (2023).
59. E. O'Day *et al.*, An RNA-binding Protein, Lin28, Recognizes and Remodels G-quartets in the MicroRNAs (miRNAs) and mRNAs It Regulates. *J. Biol. Chem.* **290**, 17909–17922 (2015).
60. A. M. Fleming *et al.*, Second harmonic generation interrogation of the endonuclease APE1 binding interaction with G-quadruplex DNA. *Anal. Chem.* **94**, 15027–15032 (2022).
61. G. Mangiapane *et al.*, Clinical significance of Apurinic/Apyrimidinic Endodeoxyribonuclease 1 and MicroRNA axis in Hepatocellular Carcinoma. *J. Clin. Transl. Hepatol.* **11**, 1291–1307 (2023).
62. D. Fantini *et al.*, APE1/Ref-1 regulates PTEN expression mediated by Egr-1. *Free Radic Res.* **42**, 20–29 (2008).
63. D. Fantini *et al.*, Critical lysine residues within the overlooked N-terminal domain of human APE1 regulate its biological functions. *Nucleic Acids Res.* **38**, 8239–8256 (2010).
64. T. A. Turunen *et al.*, Changes in nuclear and cytoplasmic microRNA distribution in response to hypoxic stress. *Sci. Rep.* **9**, 10332 (2019).
65. W. Huajun *et al.*, Clinical value of combined detection of serum APE1-Aabs and CEACAM-1 in the diagnosis of colorectal cancer. *Eur. Rev. Med. Pharmacol. Sci.* **22**, 1286–1289 (2018).
66. D. Pascut *et al.*, Serum AP-endonuclease 1 (sAPE1) as novel biomarker for hepatocellular carcinoma. *Oncotarget* **10**, 383–394 (2019).
67. S. Zhang *et al.*, Serum APE1 as a predictive marker for platinum-based chemotherapy of non-small cell lung cancer patients. *Oncotarget* **7**, 77482–77494 (2016).
68. G. Mangiapane *et al.*, Enzymatically active apurinic/apyrimidinic endodeoxyribonuclease 1 is released by mammalian cells through exosomes. *J. Biol. Chem.* **296**, 100569 (2021).
69. I. Parolini *et al.*, Intraluminal vesicle trafficking is involved in the secretion of base excision repair protein APE1. *FEBS J.* **291**, 2849–2875 (2024).
70. M. Montes, M. Huarte, 8G modifications rewire tumoral microRNAs. *Nat. Cell Biol.* **25**, 1243–1244 (2023).
71. M. C. Malfatti *et al.*, AUF1 recognizes 8-oxo-guanosine embedded in DNA and stimulates APE1 endoribonuclease activity. *Antioxid Redox Signal* **39**, 411–431 (2023).
72. T. Ishii, H. Hayakawa, T. Igawa, T. Sekiguchi, M. Sekiguchi, Specific binding of PCBP1 to heavily oxidized RNA to induce cell death. *Proc. Natl. Acad. Sci. U.S.A.* **115**, 6715–6720 (2018).
73. O. Kikin, L. D'Antonio, P. S. Bagga, QGRS Mapper: A web-based server for predicting G-quadruplexes in nucleotide sequences. *Nucleic Acids Res.* **34**, W676–W682 (2006).
74. D. Labudová, J. Hon, M. Lexa, pqsfinder web: G-quadruplex prediction using optimized pqsfinder algorithm. *Bioinformatics* **36**, 2584–2586 (2020).
75. V. Brázda *et al.*, G4Hunter web application: A web server for G-quadruplex prediction. *Bioinformatics* **35**, 3493–3495 (2019).
76. M. Kanehisa, S. Goto, KEGG: Kyoto encyclopedia of genes and genomes. *Nucleic Acids Res.* **28**, 27–30 (2000).
77. K. T. Gagnon, L. Li, B. A. Janowski, D. R. Corey, Analysis of nuclear RNA interference in human cells by subcellular fractionation and Argonaute loading. *Nat. Protoc.* **9**, 2045–2060 (2014).
78. W. Lee, M. Tonelli, J. L. Markley, NMRFAM-SPARKY: Enhanced software for biomolecular NMR spectroscopy. *Bioinformatics* **31**, 1325–1327 (2015).
79. E. F. Pettersen *et al.*, UCSF Chimera–a visualization system for exploratory research and analysis. *J. Comput. Chem.* **25**, 1605–1612 (2004).
80. M. C. Bellina *et al.*, Apurinic/Apyrimidinic Endodeoxyribonuclease 1 modulates RNA G-quadruplex folding of miR-92b and controls its expression in cancer cells - raw data. Open Science Framework. https://osf.io/jch3g/?view_only=4639cd6e2ed3447c9c7cc3496392ee83. Deposited 24 September 2024.